

On the equilibrium limit of liquid stability in pressurized aqueous systems

Arian Zarriz¹, Baptiste Journaux² ✉, Matthew J. Powell-Palm^{1,3,4} ✉

¹J. Mike Walker '66 Department of Mechanical Engineering, Texas A&M University, College Station, TX, USA

²Department of Department of Earth and Space Sciences, University of Washington, Seattle, WA, USA

³Department of Materials Science & Engineering, Texas A&M University, College Station, TX, USA

⁴Department of Biomedical Engineering, Texas A&M University, College Station, TX, USA

Correspondence:

BJ (bjournau@uw.edu)

MPP (powellpalm@tamu.edu)

Abstract:

Phase stability, and the limits thereof, are a central concern of materials thermodynamics. However, the temperature limits of equilibrium liquid stability in chemical systems have only been widely characterized under constant (typically atmospheric) pressure conditions, whereunder these limits are represented by the eutectic. At higher pressures, the eutectic will shift in both temperature and chemical composition, opening a wide thermodynamic parameter space over which the absolute limit of liquid stability, i.e., the limit under arbitrary values of the thermodynamic forces at play (here pressure and concentration), might exist. In this work, we use isochoric freezing and melting to measure this absolute limit for the first time in several binary aqueous brines, and nodding to the etymology of “eutectic”, we name it the “cenotectic” (from Greek “κοινόζ-τηξίς”, meaning “universal-melt”). We discuss the implications of our findings on ocean worlds within our solar system and cold ocean exoplanets; estimate thermodynamic limits on ice crust thickness and final ocean depth (of the cenotectic or “endgame” ocean) using measured cenotectic pressures; and finally provide a generalized thermodynamic perspective on (and definition for) this fundamental thermodynamic invariant point.

Introduction:

Multiphase liquid-solid equilibrium ranks amongst the most fundamental concepts in thermodynamics and physical chemistry, providing the foundation of modern phase diagrams, grounding thermodynamic analysis, and driving countless industrial processes. In multicomponent systems, at constant pressure, the lowest temperature at which a liquid may remain stable at equilibrium is defined as the eutectic (from Greek “εὐ-τήξις”, “easy-melt”), an invariant point in temperature-concentration (T-x) space at which the liquid will transition entirely into a mixture of solid phases. Eutectics are of crucial importance to a wide range of applications, from metallurgy to igneous rock formation, phase change thermal energy storage to cryopreservation, drug discovery to planetary science, and etc. The canonical definition of the eutectic is often considered at a fixed pressure (typically 0.1 MPa / atmospheric pressure); however, increased states of compression may substantially affect the melting curves of solids, resulting in a change of eutectic T-x coordinates. When pressure is varied, the eutectic becomes a univariant curve in P-T-x space, the trajectory of which depends upon the geometry of the liquidus curves of the contributing solid phases.

For most materials, solid phases are denser than the liquid phase, meaning these materials possess positive Clapeyron melting slopes ($dP/dT > 0$). For systems containing such solids, univariant eutectic curve (also called cotectic) temperatures will increase with increasing pressures.

Select compounds in natural science and engineering however, such as water, silicon, or gallium, have negative Clapeyron melting slopes at 0.1 MPa (i.e., select solid phases of these compounds are less dense than the liquid). In many binary systems containing these compounds, initial compression from 0.1 MPa leads to pressure-induced melting point depression, resulting in the univariant eutectic curve decreasing in temperature with increasing pressure¹. However, for all of these systems, continued compression of the liquid will eventually result in the formation of a denser solid phase (e.g., ice III, Si-II, Ga-II), thereby reversing the Clapeyron slope. In this context, the negative-Clapeyron eutectic curve for the lower pressure range will intersect a positive-Clapeyron higher-pressure melting line at an invariant point in P-T-x space.

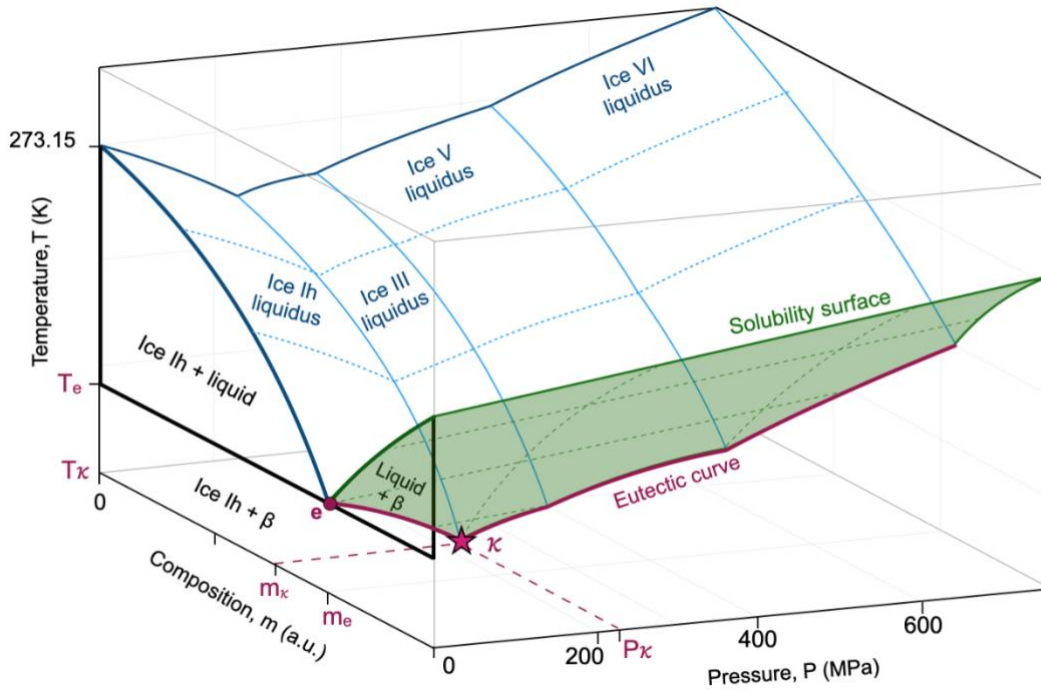


Figure 1: Conceptual pressure-temperature-concentration phase diagram for a binary solution of water and a generic salt-like solute with only one solute-bearing solid phase. The shaded green region shows the solubility surface of the solute. The eutectic at ambient pressure is marked by the magenta circle (**e**), the pressure-dependent eutectic curve is marked by the thick magenta line, and the cenotectic point (**κ**) is marked as a magenta star. m_e marks the brine concentration at the 0.1 MPa eutectic, and m_κ marks the brine concentration at the cenotectic point. P_κ, T_κ mark the pressure and temperature of the cenotectic point, which we measure in this work. Isochoric freezing/melting of brine samples of concentration m_e generally follows the pressure-temperature trajectory marked by the magenta eutectic curve between points (**e**) and (**κ**), and the cenotectic point can be identified by the change in direction of the P-T slope of this curve.

For aqueous solutions in which the eutectic in equilibrium with ice-Ih is the lowest-temperature eutectic in the phase diagram (including most solutions of salts, sugars, and other solutes that are solid at room temperature), this invariant point represents the lowest possible temperature at which a given aqueous liquid phase may remain stable at equilibrium under any P-T-x conditions, and therefore represents a fundamental property of the system. While select previous works have inadvertently observed this fundamental invariant thermodynamic point in the study of high-pressure eutectics²⁻⁴, to our knowledge, no previous study has identified or measured the invariant point itself, nor defined it as an entity distinct from other univariant transitions.

Based on the etymology of eutectic (from Greek “εὐ-τῆξις”, “easy-melt”), we propose the name cenotectic (from Greek “κοινός-τῆξις”, “universal-melt”) for this invariant point, and we illustrate it in Figure 1 as point **κ** (the Greek letter kappa), which presents a semi-quantitative P-T-x diagram for a binary system of water and a generic salt-like solute. Note that in most aqueous systems, given the geometries of the ices-liquid liquidus surfaces, this point is typically located on the ice Ih-ice III-liquid or ice Ih-ice II-liquid equilibrium boundary.

In this work, we describe first-of-their-kind experimental determinations of the precise P-T coordinates of the cenotectic points of major binary aqueous systems relevant to the planetary sciences, medical sciences, and engineering. These results are acquired via an isochoric freezing and melting approach previously established by our group¹ for the interrogation of univariant phase configurations, which we herein extend to the absolute temperature limit of aqueous liquid stability, and furthermore use to identify several potentially new high-pressure hydrate phases. We discuss the implications of this data on our evolving understanding of low-temperature aqueous thermodynamics, detail implications in planetary science for icy ocean worlds, and provide a suggested roadmap toward rapid illumination of the yet-unexplored low-temperature high-pressure parameter space for aqueous solutions. In closing, we provide a generalized and complete definition of the cenotectic, applicable to arbitrary chemical systems under the influence of any arbitrary modes of thermodynamic work.

Results:

Here we use isochoric freezing and melting¹ to measure the pressure-temperature evolution of the eutectic for eight aqueous binary solutions (Na_2CO_3 , KCl, MgSO_4 , Na_2SO_4 , Urea, NaCl, MgCl_2 , and NaHCO_3) in the temperature range 203 to 273.15K and the pressure range 250 to 0.1 MPa, identifying the P-T coordinates of the cenotectic point in six of them and pointing at new possible high-pressure hydrate phases in the remaining three (NaCl, MgCl_2 , NaHCO_3). The eutectic P-T curves for all eight solutions studied are shown in Fig. 2.

In brief, the experimental methodology consists of confining each ~5.33 mL eutectic solution sample in a custom metallic isochoric chamber free of air and fitted with a high-accuracy pressure transducer; submerging the chamber in a calibration-grade programmable circulating bath; cooling the chamber continuously to a temperature at least 30 K beneath the 0.1 MPa eutectic temperature; allowing all crystallization processes to reach steady-state (after nucleation of ice III or ice II), as indicated by constancy of the pressure signal; then warming the chamber and melting its contents in 0.5 K increments, recording the steady pressure at each temperature. Isochoric conditions allow the pressure in the system to vary freely in response to the changing volumes of emerging or receding phases, and couple the temperature and pressure according Gibbs' phase rule, which dictates that a univariant phase configuration (i.e., the three-phase eutectic in a binary solution) has only one intensive degree of freedom.

Additional details on the isochoric freezing and melting process are provided in the Methods and in Supplementary Note 1, with chamber schematics provided in Supplementary Figure S1. Example time-series pressure-temperature data of the entire isochoric freezing and melting process are provided in Supplementary Note 2. Detailed uncertainty analysis is provided in Supplementary Note 4. Additional discussion of the thermodynamic principles, merits, and drawbacks of the technique is provided in Chang et al¹.

Cenotectic measurements

After total freezing of the solution, most experiments are observed to stabilize around 210 MPa (see for example Figure S2), coincident with the solid-solid phase transitions of ice Ih-ice III and ice Ih-ice II in the studied temperature range^{5,6}. Upon warming, the pressure first remains approximately constant for some period, again consistent with the quasi-isobaric

nature of the ice Ih-ice III/II phase boundary, and we then observe two varieties of isochoric pressure-temperature curves, monotonic (Na_2CO_3 , KCl , MgSO_4 , Na_2SO_4 , and Urea), and non-monotonic (NaCl , MgCl_2 , and NaHCO_3).

For monotonic curves, shown in Figures 2.a and 2.b, as temperature increases during warming, we first observe a clear discontinuity in the slope of the P-T curve upon emergence of the liquid phase, and then a monotonic decrease in pressure as the liquid phase fraction increases along the eutectic curve. This first discontinuity is identified as the cenotectic point, the lowest temperature at which the liquid phase remains stable, and occurs at pressures consistent with the ice Ih-ice III or ice Ih-ice II transitions.

In order to precisely identify the cenotectic P-T coordinates, we fit polynomials to P-T eutectic curves colder and warmer than the apparent cenotectic point (the colder curve including ice Ih, ice II/III, and the salt-bearing solid phase; and the warmer curve including ice Ih, the salt-bearing solid phase, and the liquid) and calculated their intersection, at which all four phases may coexist. Average cenotectic pressures and temperatures across $n = 3$ trials per solution are listed in Table 1, alongside the initial concentration of the solution used, the eutectic temperature measured at atmospheric pressure, and the temperature delta between the eutectic and the cenotectic. Propagated uncertainties accounting for both experimental error and fit uncertainty are included in parentheses (details in Supplementary Note 4).

In Figure 2.a, we also compare our eutectic curve P-T results for MgSO_4 and Na_2SO_4 to those of Hogenboom and colleagues^{2,3}, which agree well and represent the only other data we were able to identify on high-pressure low-temperature eutectic equilibria for the systems studied here. Furthermore, although Hogenboom and co. did not measure the cenotectic points of these two solutions, we may estimate them by quadratically fitting the data clusters along the ice Ih eutectic and ice III eutectic curves and calculating the intersections of these fits. The cenotectic values calculated from the data of Hogenboom and co. (MgSO_4 : 211.74 MPa, 248.50 K; Na_2SO_4 : 208.34 MPa, 249.95 K) stand in strong agreement with the measurements featured in Table 1.

These literature data also highlight the distinct enhancement in resolution afforded by the isochoric freezing and melting approach, which enables continuous generation and measurement of pressure in response to continuous variation of the temperature, as compared to isobaric techniques performed at discrete isothermal-isobaric pressure-temperature steps. The results herein furthermore confirm the suspicions of Hogenboom et al. that their measurements of water- Na_2SO_4 eutectic coordinates did not reflect the equilibrium state (i.e. entered a metastable configuration) at pressures above 200 MPa.

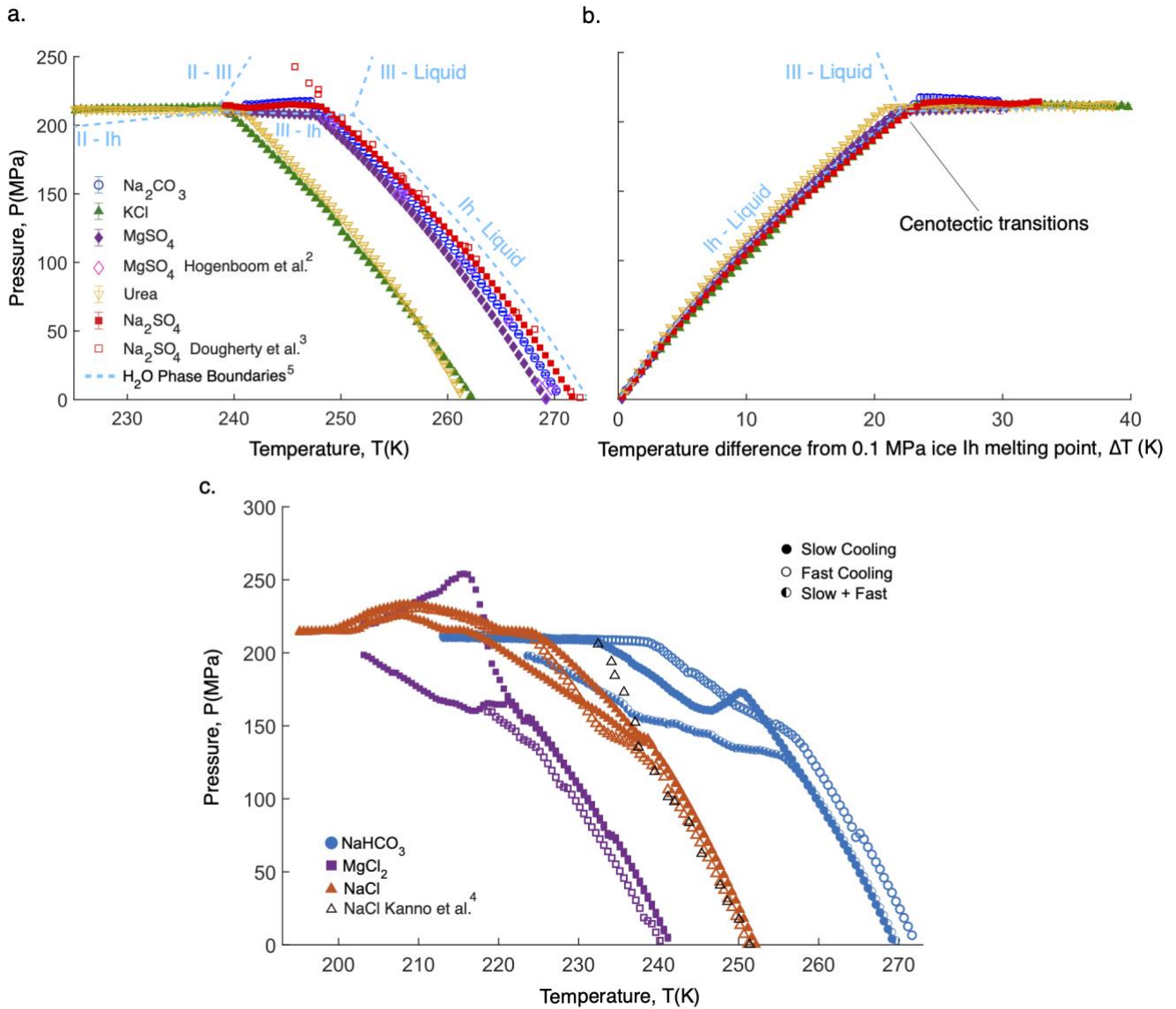


Figure 2. Binary solution eutectic pressure-temperature (P-T) profiles. *a*) P-T profiles for the five binary eutectic solutions tested that do not produce new salt-bearing solid phases at high-pressure. The cenotectic point for each solution, or the limit of liquid stability, occurs at the slope discontinuity in each curve, at which point the remaining liquid solidifies into a solid solution of ice Ih, ice III or ice II, and the salt-bearing solid phase. The phase boundaries of the pure water phase diagram (computed using the SeaFreeze thermodynamic framework⁵) are superimposed atop the data for context. *b*) the same pressure profiles plotted against the temperature delta from the melting point of ice Ih, which for each of the solutions is the atmospheric pressure eutectic point, and for pure water is 273.15K. In *a*) and *b*), markers present the mean of $n = 3$ replicate trials, and error bars show standard deviation (which is on the order of ~ 1 MPa across trials). *c*) P-T profiles for three binary eutectic solutions that do produce new (potentially metastable) salt-bearing solid phases at high-pressure. With decreasing temperature, discontinuities in the slope of the P-T eutectic curve represent phase transitions involving the salt. Each curve represents a single trial, produced via either a slow cooling, fast cooling, or combined slow and fast cooling routine (details in Methods). Further detail on these trials is available in Supplementary

Notes 2 and 3, and additional data recorded for the solutions producing intermediate phases is provided in Supplementary Figures S3-S5. Source data are provided in the Source Data file.

It should be noted that while we do not directly measure the evolution of the salt concentration in the aqueous liquid phase, based on our previous study of high-pressure binary eutectics¹, we expect that it will continuously decrease with increasing pressure, beginning at approximately the eutectic concentration (m_e in Figure 1; exact value listed in Table 1) and ending at the cenotectic concentration (m_c in Figure 1). Using the cenotectic P-T coordinates shown in Table 1, future work should aim to characterize the cenotectic salt concentration directly.

Table 1. Measured multiphase P-T equilibria for solutions exhibiting monotonic P-T eutectic curves.

Solute Salt	Initial brine concentration (Eutectic concentration at 0.1 MPa; wt %)	Eutectic Temperature at 0.1 MPa (K)	Cenotectic Temperature (K)	Temperature difference between Eutectic at 0.1 MPa and Cenotectic (K)	Cenotectic Pressure (MPa)
Na ₂ CO ₃	5.88	270.77 (0.14)	247.11 (0.48)	23.66	217.41 (1.61)
KCl	19.50	262.41 (0.16)	238.90 (0.52)	23.52	213.33 (1.58)
MgSO ₄	17.30	269.29 (0.10)	247.56 (0.34)	21.75	207.31 (0.94)
Urea	32.80	261.74 (0.18)	240.50 (0.53)	21.21	210.38 (1.24)
Na ₂ SO ₄	4.15	272.99 (0.13)	248.01 (0.54)	23.98	214.46 (1.80)

For NaCl, MgCl₂, and NaHCO₃, our ability to observe the stable ice III (or ice II below 238 K) transition and determine the cenotectic was confounded by the apparent emergence of high-pressure intermediates, some of which we anticipate may represent previously-unknown phases. P-T coordinates measured for each of these systems under different cooling protocols (see Methods) are shown individually in Figure 2.c (with additional runs shown in Supplementary Note 3), and suggest that isochoric freezing and melting may prove an effective technique for screening for new phases in low-temperature aqueous systems.

For the 23.3% NaCl solution, which begins in a eutectic configuration comprised of liquid, ice Ih, and hydrohalite (NaCl·2H₂O, or SC2), an intermediate phase transition was observed at approximately 237K / 140 MPa, remarkably close to the temperature at which Journaux and colleagues estimate the recently discovered hyper-hydrate 2NaCl·17H₂O (SC8.5) may form⁷. This second phase configuration continued without interruption to approximately 215 MPa

across trials, but achieved this pressure at between 216 and 224K depending on the run. The P-T coordinates of the initial eutectic configuration agree well with previous data from Kanno & Angell (black triangles in Fig. 2c), who observed high-pressure eutectic phenomena whilst studying pressurized homogeneous ice nucleation via differential thermal analysis in emulsified H₂O-NaCl samples⁴. They do not report an additional phase transition however, which is likely a kinetic consequence of both emulsification and miniscule sample sizes (0.04-0.08 mL), which they deploy in order to hinder heterogeneous nucleation of new phases. The large sample sizes (here 5.33 mL) deployable in isochoric freezing and melting may provide a distinct advantage in this regard, helping to ensure timely heterogeneous nucleation of new phases.

In 6.15% NaHCO₃ solution, which begins in a eutectic configuration comprised of liquid, ice Ih, and pure NaHCO₃, a phase transition was observed at approximately 255K / 130 MPa, suggesting the existence what may be the first reported hydrate for NaHCO₃, at high-pressure or otherwise. Chamber-to-chamber P-T results grow less consistent after this first phase transition, with two runs eventually unifying in pressure at 210 MPa (albeit at 232K and 238K), and the third taking a much shallower approach in temperature. The transition at 210 MPa suggests that another phase transition may occur in this 232-238K temperature range, be it within the salt-bearing solid phase or the ice phase. Future work should address the structure and stability range of these (potentially multiple) new hydrates, and may provide fundamental new insight into the hydration dynamics of NaHCO₃.

Finally, in 21.6% MgCl₂ solution, which begins in a eutectic configuration comprised of liquid, ice Ih, and MgCl₂-12H₂O, discrete phase transitions were observed in multiple runs at approximately 233K / 75 MPa and 223K / 155 MPa, after which the behaviors of the different samples diverged significantly. MgCl₂ is known for its diverse array of stable hydrate phases, with hydration numbers up to 12 observed at ambient pressure⁸. However, to our knowledge, the only hydrate reported to exist in equilibrium with ice Ih is MgCl₂-12H₂O, suggesting that the phase transitions observed here may represent previously unrealized phases.

Discussion

Role of water-ice stability in prescribing the cenotectic

Our measurements provide several key insights into the evolution of aqueous systems with pressure. Firstly, it appears that for binary salt systems that do not undergo transitions to a salt-bearing solid phase at high-pressures, the P-T coordinates of the cenotectic are dictated high-exclusively by the thermodynamics of water/ice. As shown in Fig. 2.b, the P-T evolution of each eutectic configuration from its 0.1 MPa eutectic point mirrors the P-T evolution of ice Ih and liquid water from 273.15K, consistently producing the ice III transition (which here marks the cenotectic) at approximately 22K beneath the melting point of ice Ih, and at approximately 210 MPa. This is a key finding for analysis of binary aqueous salt systems of relevance to planetary science, cryopreservation, etc., providing a general thermodynamic limit on the presence of stable equilibrium liquid. We furthermore hypothesize that if no new stable hydrate phases are present at high-pressures in *any* given aqueous salt solution, be it a binary or many-component system, this 22K rule of thumb should hold true for the temperature difference between the 0.1 MPa univariant eutectic and the cenotectic. Following this logic, as the ice Ih-III-II triple point is located around 238 K and 210 MPa, systems with 0.1 MPa eutectics > 260 K (238+22) are predicted to possess a cenotectic at the ice Ih-ice III-liquid

triple point, and systems with 0.1 MPa eutectics < 260 K are predicted to possess a cenotectic at the ice Ih-ice II-liquid triple point.

For clarity, in Figure 3, we have extended the conceptual phase diagram presented in Figure 1 to include prototypical examples of solute solubility surfaces that may correspond to these differing cenotectics, organizing them by molar solubility. Examples of low solubility (e.g. aqueous Na_2SO_4 or MgSO_4) and medium solubility (e.g. aqueous KCl or Urea) cenotectics are represented within the experimental data in Fig. 2a/b, and marked conceptually in Fig. 3 by κ_1 and κ_2 . Examples of high solubility cenotectics (occurring at the ice Ih-ice II-liquid triple point and marked by κ_3) have not been experimentally confirmed in this work, but we suggest that aqueous perchlorates may be good candidates, as they often possess very low 0.1 MPa eutectic temperatures (e.g. 236 K for NaClO_4 and 206 K for MgClO_4). For aqueous NaCl and MgCl_2 , while we observe signs of new hydrate species at high pressures that may increase the temperature of the cenotectic, it appears likely that they will yet fall beneath 238K (along the Ih-ice II-liquid triple point), considering the trends of their eutectic curves (Fig.2c).

We suspect that the general dominance of water-ice thermodynamics over the trajectory of the univariant (here binary eutectic) configuration is a function of the uniquely high phase volume difference between liquid water and ice Ih, which renders them significantly more sensitive to pressure (in this temperature range) than the salt-bearing solid phases. We emphasize however that in hypothetical aqueous systems wherein the salt-bearing solid phase boundaries may vary significantly with pressure over the same ~210 MPa range relevant to ice Ih, this 22 K rule of thumb need not necessarily hold.

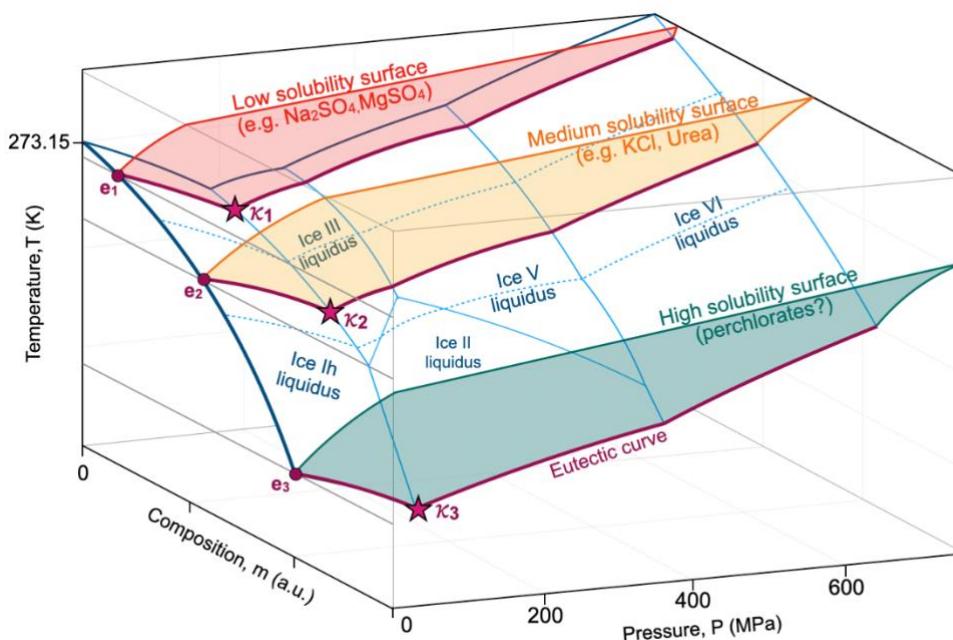


Figure 3: Conceptual pressure-temperature-concentration phase diagram depicting binary solutions of water and generic salt-like solutes of varying solubilities. A generic low solubility surface is shown in red, a generic medium solubility surface is shown in yellow, and a generic high solubility surface is shown in green. The 0.1 MPa eutectic points corresponding to each surface are marked by (e_1 , e_2 , e_3), and the cenotectics are marked by (κ_1 , κ_2 , κ_3), where increasing subscript indices correspond to increasing solubility. All other markings retain the meanings indicated in Figure 1.

Intermediate salt-based phase transitions along the eutectic curve

As shown in Fig. 2c., three binary systems that produced intermediate phase transitions within approximately 22K of their 0.1 MPa eutectic points proceeded to diverge from the eutectic trajectories of their monotonic counterparts.

Unlike in the previous solutions, these binaries showed notable sensitivity to the cooling and warming protocol employed and divergence amongst like samples, producing anomalous P-T curves. At equilibrium, a stable phase will have the highest melting temperature at a fixed pressure and composition (or conversely the highest pressure at a fixed temperature and composition). Proceeding along the eutectic curve (toward lower temperatures and higher pressures), if reaching the range of stability of a new hydrate, one should expect a discontinuity of slope in the P-T trajectory, with the value of the Clapeyron slope becoming more negative (steeper). Here we observe the opposite, with the slope becoming more positive (less steep) after discontinuity. This suggests that possible metastable phases of hydrates may have formed during cooling, and that during warming (when step-wise P-T data is recorded), these various phases may reach their metastable melting point(s) below the cenotectic temperature, therefore creating the complex isochoric path we report here.

For example, for the H₂O-NaCl system, several new hydrates have recently been reported, including NaCl·8.5(H₂O) (SC8.5), which possesses a melting point measured at 240K at 380 MPa, and an extrapolated 0.1 MPa metastable melting point at 235K⁷. Along the NaCl(aq) isochoric P-T eutectic curve we see a discontinuity of slope at approximately 140MPa and 238K. This is where one would expect SC8.5 to cross its metastable melting curve at that pressure. This illustrates how a hydrate, stable at higher pressure, can leave a clear trace as a metastable phase in an isochoric experiment. Accordingly, this suggests that the other systems with anomalous isochoric paths possess other undiscovered hydrates, potentially stable at higher pressures. This supports the hypothesis of pressure-induced hydrate structural diversity (hyper-hydration) from Journaux et al.⁷, and we expect one or multiple new hydrates to be stable at higher pressures in MgCl₂ and NaHCO₃. This underlines the power of the isochoric method to rapidly explore the fundamental thermodynamics and physical chemistry of these systems, and future experiments should investigate high-pressure stability and structure of hydrates in those systems.

Finally, it should be noted that formation of metastable intermediates confounds our ability to directly measure the stable cenotectic temperature in these chemical systems. This presents an interesting physical paradox: new hydrates encountered along the eutectic curve that originates at 0.1MPa must definitionally be stable at higher pressures than the eutectic P-T curve would provide; but as observed, they may produce metastable configurations at lower pressures. This implies that the formation of new stable hydrates, at thermodynamic equilibrium, will increase the cenotectic temperature, ushering the system to pressures at which ice II or III may form at higher temperatures (less than the 21K rule of thumb) and limiting the stability range of the liquid. Simultaneously, the formation of metastable new hydrates will decrease the cenotectic temperature, extending the temperature range over which liquid may exist by tens of degrees or more (Fig. 2c). Additional investigation into kinetic aspects of these systems (further cooling rate sensitivities, effects of different annealing temperatures, effects of spontaneous or stimulated nucleation temperatures, etc.) may yield deeper insight into their potential metastability.

Implications for materials thermodynamics and generalized definition of the cenotectic

For any thermodynamic system, under the influence of any arbitrary selection of physical or chemical thermodynamic forces (pressure, chemical potential, etc.) acting at arbitrary intensities, there exists a temperature limit to the stability of the liquid phase, which we here dub the cenotectic. For systems free of the influence of non-simple modes of thermodynamic work (e.g. magnetic work, electronic work, stress-strain work, surface work, etc.), this limit will be a function of pressure and $c - 1$ compositional variables, wherein c is the number of chemical components. For systems under the influence of the more exotic forms of thermodynamic work mentioned above, the cenotectic will depend further on one additional variable for each contributing work mode. As such, this cenotectic limit is a fundamental material property of the system, yet, outside of chemically pure systems, it has seldom (if ever) been precisely characterized.

In this work, we have measured the cenotectic for a variety of binary salty aqueous systems. However, these systems represent just one of several phenomenological profiles that the cenotectic may possess. Because mechanical (PV) work affects all thermodynamic systems, the cenotectic will always occur at the intersection of two univariant phase lines with opposite-signed Clapeyron (dP/dT) slopes, regardless of chemical complexity or the role of other thermodynamic fields. For the systems tested here, because water produces a solid phase (ice Ih) less dense than the liquid (thereby providing a negative Clapeyron slope along its liquidus curve), and because the eutectic featuring ice Ih is the lowest-temperature eutectic in the atmospheric pressure phase diagram, the cenotectic logically falls at the intersection of two univariant liquid-solid-solid equilibrium lines, one involving ice Ih (plus the salt-bearing solid phase) and the other involving an ice phase (II or III) more dense than the liquid (plus the salt-bearing solid phase). This reasoning can be applied equally to other systems with negative Clapeyron slope melting curves, for which the cenotectic can fall along the solid-solid transition to the denser phase (which is usually quasi-isobaric). We therefore predict that the cenotectic pressure can be expected to be approximately 11-12 GPa for many silicon solutions, 1.5 GPa for many gallium solutions, and 5-10 GPa for many carbon solutions.

However, for most binary material systems, which do not possess a solid phase less dense than the liquid along the eutectic curve, the negative-Clapeyron phase line leading into the phase intersection marked by the cenotectic will generally include liquid-vapor-solid equilibrium, instead of liquid-solid-solid equilibrium. Likewise, in aqueous solutions for which the lowest-temperature eutectic at atmospheric pressure does not involve ice Ih, such as methanol⁹, DMSO¹⁰, etc., the cenotectic may also occur at the intersection of a liquid-vapor-solid (negative Clapeyron slope) line and a liquid-solid-solid (positive Clapeyron slope).

Generally, the cenotectic point of a system will behave one of two ways, depending upon the densities of the phases involved. If the lowest-temperature eutectic at atmospheric pressure involves a phase less dense than the liquid, the cenotectic will likely occur at increased pressures, and generally at the intersection of negative-Clapeyron and positive-Clapeyron liquid-solid-solid equilibrium lines. This is the case applicable to all of the systems studied here, and the case we suggest should be broadly applicable to aqueous salt systems writ large. Alternatively, if the lowest-temperature eutectic at atmospheric pressure involves only phases that are denser than the liquid, the cenotectic will likely occur at decreased pressures,

and generally at the intersection of a positive-Clapeyron liquid-solid-solid and a negative-Clapeyron liquid-vapor-solid line. This appears to be the case for example in the water-methanol system⁹, for which the lowest temperature eutectic at 0.1 MPa does not include ice Ih, but instead solid methanol and its monohydrate. Note however that for systems with multiple eutectics at similar temperatures (such as water-DMSO¹⁰), the specific pressure-dependences of the solid phases involved may affect which 0.1 MPa eutectic the cenotectic will originate from, and an *a priori* determination of the phases involved may not be feasible.

It must also be noted that the number of phases present in the univariant phase lines that intersect to form the cenotectic will increase with the number of chemical components in the system, per the classical Gibbs Phase Rule, and with the number of additional thermodynamic fields (strain, magnetic, electric, etc.) acting upon the system, per the Generalized Gibbs Phase rule¹¹, leaving many exciting multiphase configurations to characterize across varying thermodynamic systems.

We suggest that establishment and exploration (both experimental and theoretical) of the cenotectic concept is vital to rigorous understanding of the thermodynamics of modern materials systems, which exist under increasingly complex chemical-thermodynamic conditions and produce increasingly rich multi-phase equilibria¹²⁻¹⁵. For the benefit of the modern student of thermodynamics, we thus conclude our thermodynamic discussion with a formal definition of the cenotectic:

The cenotectic is the invariant point occurring at the lowest temperature at which the liquid phase, for any value of concentration, pressure, or other thermodynamic forces acting on the system, remains in stable equilibrium.

Additional discussion (and a mathematical description) of this definition within the context of Gibbs Phase Rule is provided in Supplementary Note 5.

Implications for planetary science

The cenotectic concept has fascinating applications in planetary science, especially for cold water-rich worlds like the icy moons of the outer solar system and ocean exoplanets. In icy worlds such as Europa, Enceladus, Titan, Ganymede, Ceres, Pluto and potentially moons of Uranus Ariel, Umbriel, Titania and Oberon¹⁶⁻¹⁸, the eutectic behavior controls the stability of brines in the icy crust. This particularly affects the circulation of salty fluids and the formation of mushy layers (Figure 3) at the uppermost ocean boundaries, which may provide habitable niches for potential extraterrestrial life¹⁹⁻²¹. With increasing pressure deeper within the ice Ih crust, the temperature of the eutectic will decrease (Fig. 4). Several studies in recent years have underlined the importance of brine percolation and brine connectivity in vertical transport through the ice crust under chaos regions²², double ridge formations²³, or impacts and cryo-volcanism^{20,24,25}. The extent to which brines formed near the surface can percolate through the ice shell by various mechanisms and act as nutrient sources for the underlying oceanic habitat is *in-fine* controlled by the eutectic coordinates (Fig. 4). The present work allows us to demonstrate that for a pressure of the bottom of the icy shell of 50 MPa^{17,26} eutectic temperature of aqueous systems can be depressed by up to 4-5 K compared to its 0.1 MPa value. This difference is significant, and could enhance fluid circulation in thick ice crusts^{22,27}, further facilitating vertical transport of oxidant/nutrients from the surface to the ocean. The

high-pressure behavior of the eutectic is also relevant to the base of the ice shell, especially in controlling the formation, thickness, and chemical gradients of ocean interface mush^{28,29} (Fig. 4), and possible briny habitats¹⁹.

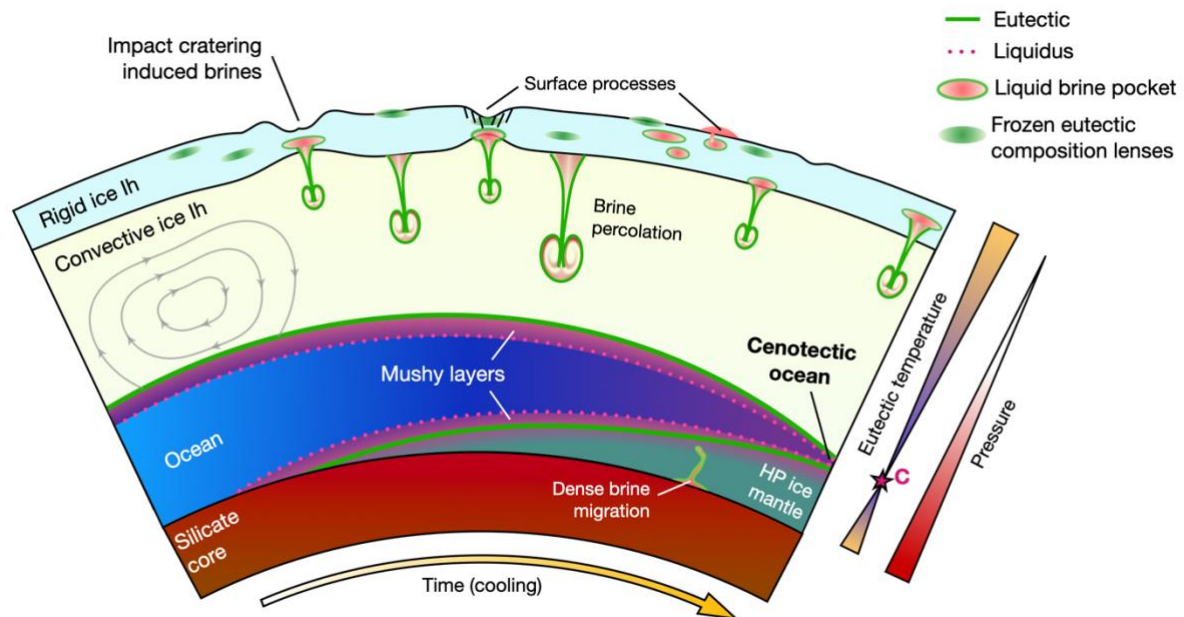


Figure 4. Schematic interior structure of an icy moon and the various geological processes involving the eutectic and cenotectic. These processes include but are not limited to brine pocket migrations, percolation, and possible eruptions (eutectic), and freezing of the hydrosphere from above (ice Ih) and below (high-pressure ices) that results in the cenotectic ocean. Ice Ih layer relative thickness is exaggerated for clarity.

The behavior of the eutectic curve at pressures higher than the cenotectic, in equilibrium with high-pressure ice polymorphs, remains to be studied with other techniques. Nonetheless, a reasonable assumption is to expect a similar behavior to that at low pressure, i.e. following the overall shape of the high-pressure ices melting curves with a given ΔT , if no high-pressure hydrates are present (Fig. 2b). For aqueous salt systems with cenotectic temperatures colder than 238 K, ice II should form, and the eutectic will follow the ice II-aqueous fluid melting line, which remains to be measured experimentally for relevant solutions. To our knowledge, ice II melting curves are only available for a few select solutes, including aqueous ammonia and aqueous methanol^{9,30}.

For large icy ocean worlds with high-pressure ices (e.g. Ganymede, Titan, Callisto) and ocean exoplanets²⁶, the coordinates of the eutectic curve will also control the circulation of metamorphic fluids or fluids from hydrothermalism through the high-pressure ice mantle, and dictate the possibility of vertical exchange of nutrients from the rocky core towards the ocean (Fig. 4). These processes and implications for geological evolution and habitability of these large moons are discussed in detail in references^{31–36}.

Finally, the cenotectic plays a central role in the “endgame” of planetary oceans. As large water-rich planetary bodies cool over geologic timescales, or with loss of internal heating such as tidal dissipation or radiogenic heating, their oceans will gradually freeze from top and bottom (Fig.4), until complete solidification is achieved. This effect is particularly interesting in the case of large icy moons like Ganymede, Callisto and Titan, but also for cold ocean

exoplanets like trappist 1e-g, and water-rich rogue exoplanets. Formation of a cenotectic ocean (i.e. an ocean existing at the coldest temperature at which the aqueous liquid will remain stable) could happen in the case that the aqueous solution stays buoyant compared to high-pressure ices, which depends on the solute molar mass and the composition of the eutectic. Otherwise the brine could be transported downward and may form dense basal oceans, as predicted for NaCl and MgSO₄ brines³⁶⁻³⁸. This important density inversion effect, which could control the distribution of aqueous reservoirs in water-rich planetary bodies, requires further investigation into the composition and density of aqueous systems along the eutectic and at the cenotectic. In the following discussion we assume that the brine at the cenotectic composition remains buoyant compared to high-pressure ices, as could be expected with the presence of ammonia, for example. We also assume that all of the chemical constituents dominating the composition of these icy oceans possess high-pressure cenotectics, like the salt systems studied here.

For cold water-rich planetary bodies, the last remnant aqueous liquid layer will occur at the depth corresponding to the pressure of the cenotectic (P_c), as shown in the present study to be around 210 MPa. In Fig. 5, this cenotectic depth z_c of the last ocean is presented as a function of gravity, and discrete values are reported in Table 2. Cenotectic depth is estimated using the formula $z_c = P_c / (\rho \cdot g)$, with the density ρ of the overlying ice taken at 930 kg/m³ (the average value for an adiabatic thermal profile in an ice Ih crust is around 250K²⁶, and g taken as the surface gravitational acceleration of the planetary body³⁹. Bodies with smaller gravity will have their last remaining aqueous liquid at greater depth, over 150 km for all large icy moons in our solar system. Small objects like Ceres, Pluto, and others are omitted here, as the calculated depth of the cenotectic is shallower than the estimated thickness of their hydrospheres. For Europa, the depth of the cenotectic roughly corresponds to the estimated thickness of its hydrosphere. For larger icy moons, the final ocean will be sandwiched between layers of ice Ih and ice III or ice II, depending on the precise composition of the remaining aqueous liquid. Interestingly, the depth of the cenotectic also provides the absolute maximum upper limit for the ice crust thickness if an ocean is present, which is 172 km for Titan, and 158 km for Ganymede. For larger bodies with larger gravitational acceleration, such as water rich exoplanets, the depth of the final ocean will be shallower, with depth ranging from 28 km for TRAPPIST-1 e to 9.7km for LHS 1140 b, implying much thinner maximum ice Ih crust (<30km) for cold ocean super earths.

Table 2: Cenotectic depth for various relevant icy moons of our solar system and ocean exoplanet candidates with effective surface temperatures below 273K.

Object	Surface Gravity (m/s ²)	Depth of the cenotectic (km) (i.e. last ocean)
Callisto	1.24	182
Titan	1.35	167
Europa	1.32	172

Ganymede	1.43	158
TRAPPIST-1 e	7.98	28
TRAPPIST-1 f	9.41	24
1g _E exoplanet	9.81	23
Teegarden's Star c	10.04	22.5
TRAPPIST-1 g	10.12	22.3
Proxima Cen b	10.6	21.3
GJ 667 C f	11.82	19.1
GJ 667 C e	11.82	19.1
GJ 1061 d	12.14	18.6
Keppler-186 f	12.23	18.5
Keppler 2-18b	12.43	18.2
Keppler-442 b	12.68	17.8
Keppler-1229 b	12.68	17.8
LHS 1140 b	23.22	9.7

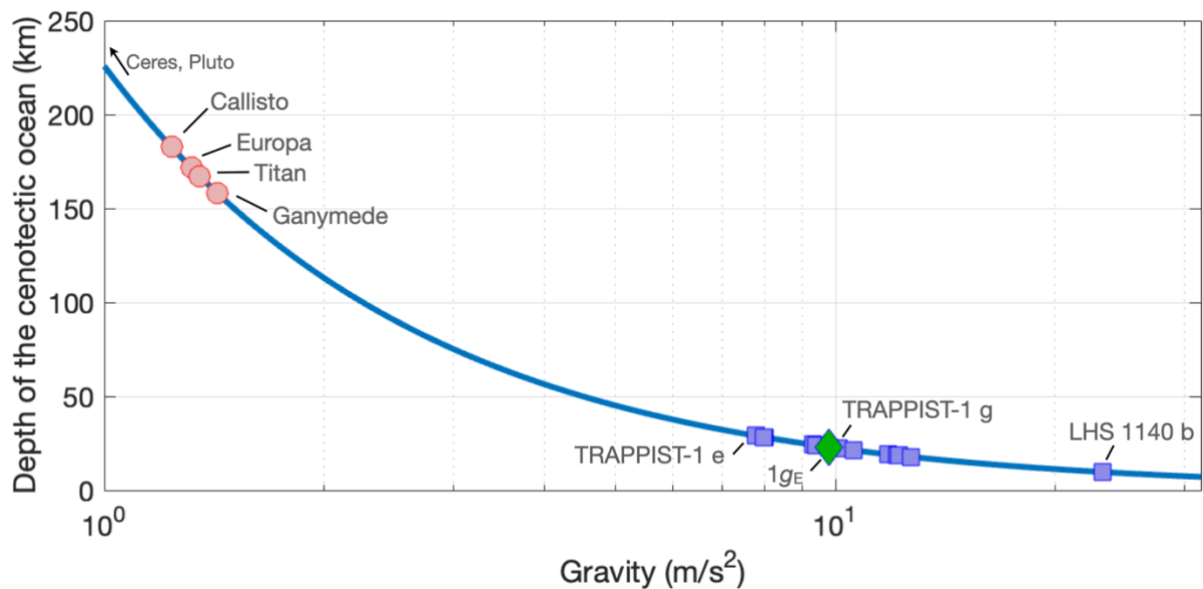


Figure 5: Evolution of the final depth of the cenotectic ocean (cenotectic depth) for different planetary bodies from our solar system and ocean exoplanet candidates. The cenotectic ocean is the ocean occurring at the depth where the last liquid layer remains stable during the freezing of the hydrosphere over the course of geological time. Surface gravity values taken from Ojha et al ³⁹.

Future work and perspective on the cenotectic

The cenotectic, or the invariant point defining the lowest temperature at which a liquid remains stable under any possible values of concentration, pressure, and other thermodynamic parameters affecting the system, is an important concept in material characterization of complex multiphase systems. As the thermodynamic and compositional parameter spaces of interest to the research community grow ever larger, identifying globally limiting behaviors becomes increasingly essential, and we suggest that the cenotectic concept may help to establish definite and fundamental limits on liquid phase equilibria. With that in mind, future research should aim not only to measure the cenotectic limits of many other chemical systems (including those aqueous systems relevant to potential high-pressure low-temperature applications such as cryopreservation^{40,41,42}), but to further refine and explore the concept itself, with the goal of ever deeper understanding of the physical limits of material systems.

Methods:

Isochoric Freezing and Melting Process

In order to identify the temperature limit of liquid stability in the aqueous solutions explored herein, we extended the isochoric freezing and melting technique reported previously by Chang et al¹ to deeper temperatures. In brief, 5.33 mL aqueous samples mixed at the atmospheric-pressure eutectic concentration were confined absent air within a custom Al7075 isochoric chamber fitted with a high-pressure transducer (ESI Technology Inc). By constraining the total volume of the binary system and allowing the pressure to vary freely, we create a thermodynamic environment in which the 3-phase equilibrium present in the eutectic configuration is prescribed by a single intensive thermodynamic degree of freedom. As such, temperature and pressure are coupled within the chamber, and simple control of the temperature enables simultaneous measurement of the equilibrium temperature and pressure. Further experimental details and chamber schematics are provided in Supplementary Notes 1-3, and described below, with full experimental procedures provided to ensure reproducibility.

Freezing process

Two high-accuracy recirculating cooling baths were employed for isochoric testing, a PolyScience AP15R-40 with a minimum working temperature of 243.15K and a Fluke Calibration 7380 with a minimum working temperature of 193.15K. The latter was utilized for solutions with phase transitions lower than 243.15K (including all those exhibiting intermediate high-pressure hydrate phases), and the former for all others. For each solution, three replicate samples in identical chambers were studied, and the chambers are submerged completely within the cooling bath fluid to ensure uniformity of temperature. More details on the cooling methodology and equipment are available in Supplementary Note 1, and a sample cooling profile is shown in Supplementary Note 2.

For solutions without intermediate high-pressure hydrates phases (i.e. those with monotonic P-T trajectories), the chambers are plunged into a bath pre-cooled to at least 30K beneath the 0.1 MPa eutectic temperature of the solution, monitored until the ice III/II transition is observed (indicated upon cooling by a precipitous collapse in pressure to approximately 210 MPa; see Fig. S2), and then allowed to further equilibrate until the pressure stabilizes to <0.1 MPa/min variation (typically 1-2 hours).

For solutions found to host intermediate high-pressure hydrate phases (NaCl, NaHCO₃, and MgCl₂, i.e. those with non-monotonic P-T trajectories), contrary to their less phase-diverse counterparts, preliminary testing showed broad varieties in behavior sample-to-sample, leading us to believe that metastable configurations were being produced and that a more gradual cooling approach may be necessary. As such, for the protocol identified as Slow Cooling in Fig. 2c., the chambers were pre-cooled only to 273.15K, and the bath temperature was then decreased by 1K every 10 minutes. The protocol identified as Fast Cooling follows the approach described above for solutions without high-pressure intermediates, wherein the chamber is submerged directly into liquid pre-cooled to the minimum temperature of the run, with the exception that pressure equilibration after the ice III/II transition typically required 6-8 hours. In order to demonstrate the hallmark dependence of metastable configurations on thermal history, a combined slow-fast cooling approach was also tested, which incorporated a pseudo-annealing logic. In this process, the temperature was incrementally lowered at a rate of 1K per 10 minutes until the intermediate hydrate was detected, then raised 5K above the observed transition temperature, and cooled once more at a rate of 0.5K/min to the cenotectic point.

See Supplementary Note 2 for example time-series data on the freezing process, and Supplementary Note 3 for additional data on solutions with intermediate hydrates.

Melting process

For all solutions, after completion of the cooling process, the system is heated in discrete increments of 0.5K, with time increments chosen based on the heat transfer characteristics of each bath to produce steady steady-state P-T data by the end of each step (at which point the data is sampled), as indicated by a <0.1 MPa/min evolution of the pressure. Additional equipment details are available in Supplementary Notes 1 and 2, and an example cooling-warming profile is shown in Figure S2. The steady pressure and temperature are recorded at the end of each step, and this pressure-temperature data provides the P-T curves shown in Fig. 2.

Eutectic and Cenotectic Point Identification

In order to extract more precise cenotectic points from the P-T data shown in Fig.2.a, second-order polynomials were fit to the data above and below the apparent cenotectic temperature (as indicated by the discontinuity in the slope the P-T curve) using the polyfit() function in MATLAB 2023b, and their intersection provided the cenotectic temperatures/pressures reported in Table 1.

Similarly, following the approach of Chang et al.¹, the intersection of the higher-temperature fitted polynomial curve with the 0.1 MPa isobar identifies the atmospheric pressure eutectic temperature of system.

Propagating uncertainty analysis was performed to account for uncertainty in both the experimental setup and the fitting procedure, and is described in detail in Supplementary Note 4.

Data Availability Statement: All data reported herein are available in tabular form in the Source Data. Any additional information sought may be requested from the corresponding authors.

Code Availability Statement: All code employed for the analysis of data herein is available upon request to the corresponding authors. We will note however that only standard MATLAB 2023b curve fitting functions were employed, and no custom scripts were developed for analysis.

References:

1. Chang, B. *et al.* On the pressure dependence of salty aqueous eutectics. *Cell Reports Phys. Sci.* **3**, 100856 (2022).
2. Hogenboom, D. L., Kargel, J. S., Ganasan, J. P. & Lee, L. Magnesium sulfate-water to 400 mpa using a novel piezometer: Densities, phase equilibria, and planetological implications. *Icarus* **115**, (1995).
3. Dougherty, A. J. ; Avidon, J. A. ; Hogenboom, D. L. ; Kargel, J. S. Eutectic Temperatures for Low and High Pressure Phases of Sodium Sulfate Hydrates with Applications to Europa. in *43rd Lunar and Planetary Science Conference, LPI Contribution No. 1659, id.2321* (2012).
4. Kanno, H. & Angell, C. A. Homogeneous nucleation and glass formation in aqueous alkali halide solutions at high pressures. *J. Phys. Chem.* **81**, 2639–2643 (1977).
5. Journaux, B. *et al.* Holistic Approach for Studying Planetary Hydrospheres: Gibbs Representation of Ices Thermodynamics, Elasticity, and the Water Phase Diagram to 2,300 MPa. *J. Geophys. Res. Planets* **125**, (2020).
6. Dunaeva, A. N., Antsyshkin, D. V. & Kuskov, O. L. Phase diagram of H₂O: Thermodynamic functions of the phase transitions of high-pressure ices. *Sol. Syst. Res.* **44**, 202–222 (2010).
7. Journaux, B. *et al.* On the identification of hyperhydrated sodium chloride hydrates, stable at icy moon conditions. *Proc. Natl. Acad. Sci.* **120**, (2023).
8. Yamashita, K., Komatsu, K., Hattori, T., Machida, S. & Kagi, H. Crystal structure of a high-pressure phase of magnesium chloride hexahydrate determined by *in-situ* X-ray and neutron diffraction methods. *Acta Crystallogr. Sect. C Struct. Chem.* **75**, 1605–1612 (2019).
9. Dougherty, A. J. *et al.* The Liquidus Temperature for Methanol-Water Mixtures at High Pressure and Low Temperature, With Application to Titan. *J. Geophys. Res. Planets* **123**, 3080–3087 (2018).
10. RASMUSSEN, D. H. & MACKENZIE, A. P. Phase Diagram for the System Water–Dimethylsulphoxide. *Nature* **220**, 1315–1317 (1968).
11. Sun, W. & Powell-Palm, M. J. Generalized Gibbs’ Phase Rule. (2021).
12. Potticary, J. *et al.* An unforeseen polymorph of coronene by the application of magnetic fields during crystal growth. *Nat. Commun.* (2016) doi:10.1038/ncomms11555.

13. Kitchaev, D. A., Dacek, S. T., Sun, W. & Ceder, G. Thermodynamics of Phase Selection in MnO₂ Framework Structures through Alkali Intercalation and Hydration. *J. Am. Chem. Soc.* (2017) doi:10.1021/jacs.6b11301.
14. Aber, J. E., Arnold, S., Garetz, B. A. & Myerson, A. S. Strong dc electric field applied to supersaturated aqueous glycine solution induces nucleation of the γ polymorph. *Phys. Rev. Lett.* (2005) doi:10.1103/PhysRevLett.94.145503.
15. Bianchini, M. *et al.* The interplay between thermodynamics and kinetics in the solid-state synthesis of layered oxides. *Nat. Mater.* **19**, (2020).
16. Nimmo, F. & Pappalardo, R. T. Ocean worlds in the outer solar system. *Journal of Geophysical Research: Planets* vol. 121 (2016).
17. Vance, S. D. *et al.* Geophysical Investigations of Habitability in Ice-Covered Ocean Worlds. *J. Geophys. Res. Planets* **123**, (2018).
18. Castillo-Rogez, J. *et al.* Compositions and Interior Structures of the Large Moons of Uranus and Implications for Future Spacecraft Observations. *J. Geophys. Res. Planets* **128**, (2023).
19. Wolfenbarger, N. S., Fox-Powell, M. G., Buffo, J. J., Soderlund, K. M. & Blankenship, D. D. Brine Volume Fraction as a Habitability Metric for Europa's Ice Shell. *Geophys. Res. Lett.* **49**, (2022).
20. Steinbrügge, G. *et al.* Brine Migration and Impact-Induced Cryovolcanism on Europa. *Geophys. Res. Lett.* **47**, (2020).
21. Vance, S. D. *et al.* Investigating Europa's Habitability with the Europa Clipper. *Space Sci. Rev.* **219**, 81 (2023).
22. Hesse, M. A., Jordan, J. S., Vance, S. D. & Oza, A. V. Downward Oxidant Transport Through Europa's Ice Shell by Density-Driven Brine Percolation. *Geophys. Res. Lett.* **49**, (2022).
23. Culberg, R., Schroeder, D. M. & Steinbrügge, G. Double ridge formation over shallow water sills on Jupiter's moon Europa. *Nat. Commun.* **13**, (2022).
24. Lesage, E., Massol, H., Howell, S. M. & Schmidt, F. Simulation of Freezing Cryomagma Reservoirs in Viscoelastic Ice Shells. *Planet. Sci. J.* **3**, (2022).
25. Lesage, E., Massol, H. & Schmidt, F. Cryomagma ascent on Europa. *Icarus* **335**, (2020).
26. Journaux, B. *et al.* Large Ocean Worlds with High-Pressure Ices. *Space Sci. Rev.* **216**, 7 (2020).
27. Kalousová, K., Souček, O., Tobie, G., Choblet, G. & Čadež, O. Ice melting and downward transport of meltwater by two-phase flow in Europa's ice shell. *J. Geophys. Res. Planets* **119**, (2014).
28. Buffo, J. J., Schmidt, B. E., Huber, C. & Meyer, C. R. Characterizing the ice-ocean interface of icy worlds: A theoretical approach. *Icarus* **360**, (2021).
29. Buffo, J. J., Schmidt, B. E., Huber, C. & Walker, C. C. Entrainment and Dynamics of

- Ocean-Derived Impurities Within Europa's Ice Shell. *J. Geophys. Res. Planets* **125**, (2020).
30. Choukroun, M. & Grasset, O. Thermodynamic data and modeling of the water and ammonia-water phase diagrams up to 2.2 GPa for planetary geophysics. *J. Chem. Phys.* **133**, (2010).
 31. Journaux, B. *et al.* Salt partitioning between water and high-pressure ices. Implication for the dynamics and habitability of icy moons and water-rich planetary bodies. *Earth Planet. Sci. Lett.* **463**, (2017).
 32. Choblet, G., Tobie, G., Sotin, C., Kalousová, K. & Grasset, O. Heat transport in the high-pressure ice mantle of large icy moons. *Icarus* **285**, (2017).
 33. Kalousová, K., Sotin, C., Choblet, G., Tobie, G. & Grasset, O. Two-phase convection in Ganymede's high-pressure ice layer — Implications for its geological evolution. *Icarus* **299**, (2018).
 34. Lebec, L., Labrosse, S., Morison, A. & Tackley, P. J. Scaling of convection in high-pressure ice layers of large icy moons and implications for habitability. *Icarus* **396**, (2023).
 35. Hernandez, J. A., Caracas, R. & Labrosse, S. Stability of high-temperature salty ice suggests electrolyte permeability in water-rich exoplanet icy mantles. *Nat. Commun.* **13**, (2022).
 36. Journaux, B. Salty ice and the dilemma of ocean exoplanet habitability. *Nature Communications* vol. 13 (2022).
 37. Journaux, B., Daniel, I., Caracas, R., Montagnac, G. & Cardon, H. Influence of NaCl on ice VI and ice VII melting curves up to 6GPa, implications for large icy moons. *Icarus* **226**, (2013).
 38. Vance, S. & Brown, J. M. Thermodynamic properties of aqueous MgSO₄ to 800MPa at temperatures from -20 to 100°C and concentrations to 2.5molkg⁻¹ from sound speeds, with applications to icy world oceans. *Geochim. Cosmochim. Acta* **110**, 176–189 (2013).
 39. Ojha, L., Troncone, B., Buffo, J., Journaux, B. & McDonald, G. Liquid water on cold exo-Earths via basal melting of ice sheets. *Nat. Commun.* **13**, 7521 (2022).
 40. Joules, A., Burrows, T., I. Dosa, P. & Hubel, A. Characterization of eutectic mixtures of sugars and sugar-alcohols for cryopreservation. *J. Mol. Liq.* **371**, 120937 (2023).
 41. Powell-Palm, M. J. *et al.* Cryopreservation and revival of Hawaiian stony corals using isochoric vitrification. *Nat. Commun.* **14**, 4859 (2023).
 42. Fahy, G. M., MacFarlane, D. R., Angell, C. A. & Meryman, H. T. Vitrification as an approach to cryopreservation. *Cryobiology* **21**, 407–26 (1984).

Acknowledgements: The authors would like to thank Claire Miehler of the University of Southern California for her linguistic expertise, and suggestion of the term cenotectic. The authors would also like to thank Dr. Thomas Driesner for his invaluable feedback on the

manuscript and figures. BJ acknowledges the financial support provided by NSF through "The Chemistry of Aqueous Carbonic Fluids in Subduction" grant (HD1WMN6945W6), the NASA Astrobiology Institute through the Titan and Beyond node (17-NAI82-17) and the NASA Precursor Science Investigations for Europa grant (22-PSIE22_2-0024). A.Z. and MPP acknowledge funding from the NSF Engineering Research Center for Advanced Technologies for Preservation of Biological Systems (ATP-Bio) NSF EEC #1941543.

Author Contributions: M.P.P. and B.J. developed the cenotectic concept and conceived the study. A.Z. performed all experiments and data analysis, and contributed key conceptual insights. M.P.P. supervised all experimental work and analysis. B.J. performed the planetary science analyses and supervised analysis of all experimental data. All authors contributed to writing and review of the manuscript.

Competing Interests Statement: The authors acknowledge no competing or conflicting interests.

Supplementary Information

On the equilibrium limit of liquid stability in pressurized aqueous systems

Arian Zarriz¹, Baptiste Journaux², Matthew J. Powell-Palm^{1,3,4}

¹J. Mike Walker '66 Department of Mechanical Engineering, Texas A&M University, College Station, TX, USA

²Department of Department of Earth and Space Sciences, University of Washington, Seattle, WA, USA

³Department of Materials Science & Engineering, Texas A&M University, College Station, TX, USA

⁴Department of Biomedical Engineering, Texas A&M University, College Station, TX, USA

Correspondence:

BJ (bjournau@uw.edu)

MPP (powellpalm@tamu.edu)

This PDF file includes:

Supplementary Notes S1-S5

Supplementary Figures S1 to S6

Supplementary Table S1

Supplementary References

Supplementary Note 1. Isochoric Freezing and Melting Methodology

The isochoric freezing approach employed here is detailed in the main text and in Chang et al. (main text reference 1), but for the aid of the reader seeking to employ isochoric freezing, we will provide further commentary on the methodology herein.

Isochoric freezing and melting is a thermo-volumetric method used to investigate the phase transitions and equilibria of aqueous solutions. By constraining the volume and concentration of a eutectic binary solution, per Gibbs Phase Rule, the system is forced into a 1-DoF thermodynamic configuration, wherein its equilibrium is fully prescribed by one intensive variable. In practice, the experimentalist controls the temperature, allowing the pressure to respond per Le Chatelier's principle and recording it.

For the binary solutions studied here, the isochoric freezing and melting process proceeds as follows. First, a solution at the 0.1 MPa eutectic concentration is prepared. We used the literature values of atmospheric eutectic concentration listed in Table S1. We note that experimental uncertainty in the initial concentration of the solution will affect the relative phase fractions of the phases present in the eutectic assemblage, but will not substantially affect the P-T trajectory of the equilibrium curve, because there is only one intensive thermodynamic degree of freedom.

This liquid is then loaded (absent any air bubbles) into a rigid pressure-bearing Al7075 isochoric chamber (internal volume 5.33 mL) equipped with an ESI GD4200-USB-4000-DE digital pressure transducer (Figs. S1.a and S1.b). These transducers enable high-fidelity pressure measurements up to 400 MPa, at a sampling frequency of 1 Hz. They are operated via a proprietary "ESI-USB" data acquisition software available from the company.

Upon filling the chamber, the pressure transducer is threaded into the chamber and torqued down to 45 N.m. This torque value ensures effective chamber closure via metal-on-metal surface sealing (as labeled in Figure S1.b), while preventing undue stress on the sensor housing.

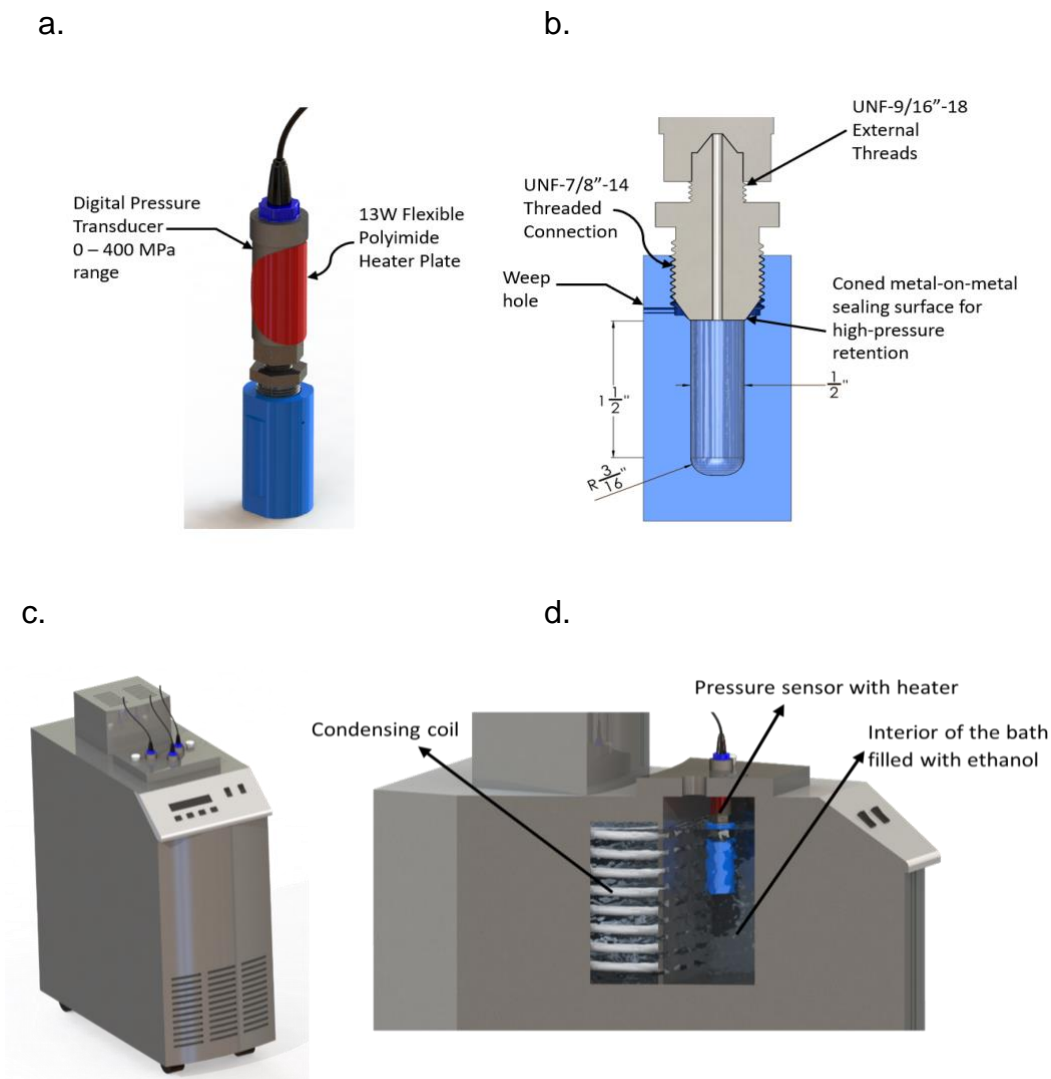
Supplementary Table 1. Atmospheric eutectic concentration for different binary solutions

Solute	Eutectic concentration (wt%)	Reference
Na₂CO₃	5.88	<i>Pascual, M., et al.¹</i>
KCl	19.50	<i>Li, Gang, et al.²</i>
MgSO₄	17.30	<i>Pillay, Venasan, et al.³</i>
Urea	32.80	<i>Yuan, Lina, et al.⁴</i>
Na₂SO₄	4.15	<i>González Díaz, C., et al.⁵</i>
NaCl	23.30	<i>Journaux et al., Drebushchak et al.⁶</i>
NaHCO₃	6.15	<i>Pascual, M., et al.¹</i>
MgCl₂	21.60	<i>Ketcham, S. A. et al.⁷, González Díaz, C., et al.⁵</i>

To maintain controlled temperature conditions for the electronics housed within the pressure transducers during the experiment (independent of the temperature of the chamber/sample), a 13W polyimide film heater with a 70 mm diameter is affixed to each pressure sensor. These heaters are regulated by a simple thermal relay responding to the observed temperature of the transducer's electronics housing, and they are set to maintain a constant temperature of $306.15 \pm 0.5\text{K}$. The relays are powered by a generic 12V DC power supply.

A 3D-printed lid was subsequently constructed to enable mounting of three chambers simultaneously in the bath, facilitating both total immersion of the isochoric chambers within the cooling fluid and insulation of the pressure transducer electronics housing above (Figure S1.d).

Two cooling baths were employed, as described in the main text. A PolyScience AP15R-40 bath was employed for binary solutions with ice-III transition temperatures higher than 243.15K, while a 7380 Fluke ultra-low temperature bath was utilized to achieve lower temperatures, reaching as low as 193.15K. This setup enabled high-throughput data collection for various binary solutions.



Supplementary Figure 1: Isochoric freezing and melting assembly. a) 3D render of Al7075 isochoric chamber (blue) and pressure transducer assembly, b) 2D cross-section of isochoric chamber and pressure transducer assembly, c, d) 3D renders of the fully assembled cooling bath (Fluke), chamber, and pressure transducer assembly.

Cooling and warming processes were programmed using on-board software for the PolyScience bath, and via MATLAB for the Fluke bath. The temperature within the bath was also recorded using a calibration-grade Fluke stick thermometer, which was submerged in the bath near the chambers to ensure precise temperature measurement.

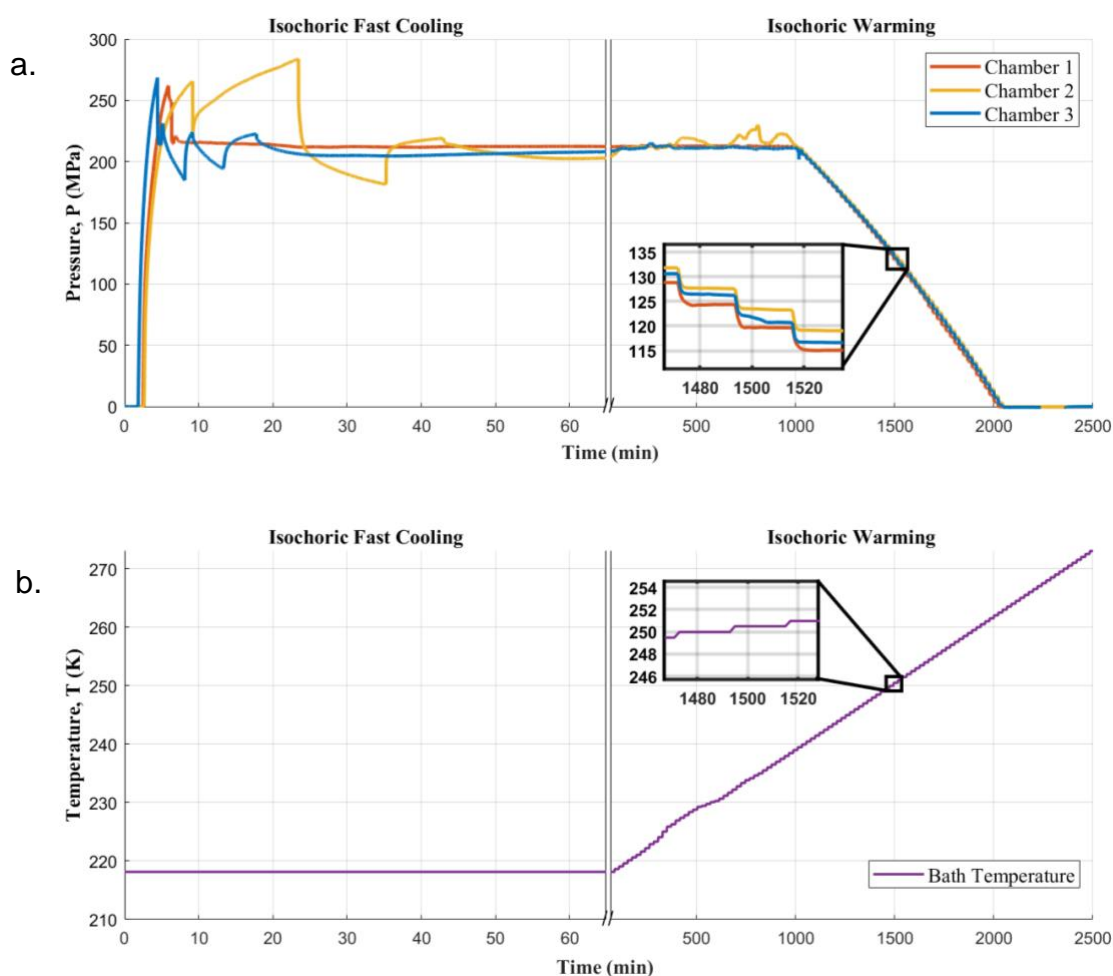
The PolyScience AP15R-40 bath was filled with a solution of water and 60% w/w ethylene glycol, in a total volume of 15 liters, per manufacturer specifications. The manufacturer-rated temperature accuracy of this bath at steady state is 0.005 °C. The large volume and high viscosity of this coolant provided a relatively high thermal resistance and relatively low cooling power to the chambers, necessitating 45 minute warming steps per 0.5K warming increment to guarantee steady-state pressure (<0.1

MPa/min). We note that this cooling bath and warming time step are identical to those employed by Chang et al. for the same protocol.

The Fluke bath was filled with a solution of water and 95% w/w ethanol, per manufacturer specifications. The manufacturer-rated temperature accuracy of this bath at steady state is 0.005 °C. The lower solution viscosity and volume as compared to the PolyScience bath provided considerably higher cooling power and faster heat transfer, necessitating 20 minute steps per 0.5K warming increment to guarantee steady-state pressure (<0.1 MPa/min).

Supplementary Note 2. Example time-series pressure-temperature data

In order to obtain equilibrium data with the highest degree of confidence possible, the P-T coordinates reported in the main text were acquired upon slow warming of the solutions. However, the general phenomenology of the cooling process may be of interest to the reader seeking to perform isochoric experiments, and we thus provide a typical cooling and warming profile below.



Supplementary Figure 2. Sample fast cooling and standard warming protocol for KCl. a) Pressure-Time profile in three chambers under fast cooling protocol and slow warming with 0.5K per 20 minutes (Fluke bath). b) Measured Temperature-Time profile in the same.

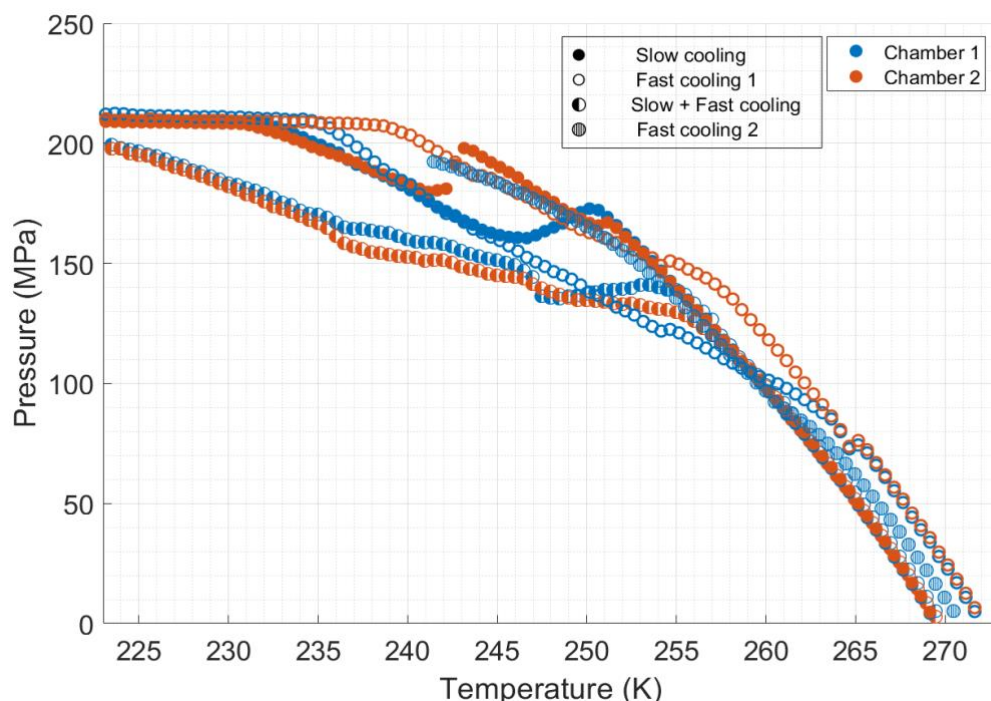
During the fast-cooling process depicted in Figure S2, with the bath set to 218.15K, two phase transition events are observed. In the first five minutes of cooling, the chamber pressures increase rapidly, which is compatible with growth of larger-volume ice Ih. It notably overshoots the ice Ih-II solid-solid phase transition around 210 MPa, producing a metastable ice-Ih liquid brine assemblage. Subsequently, we observe large drops in pressure followed by strong pressure fluctuations suggesting the formation of denser phases. Considering the pressure and temperature, it is reasonable to associate these variations with the formation of dense KCl salt and/or ice II for pressure drops, and ice Ih for pressure increases, until reaching an equilibrium assemblage. The significant variations between each chamber in the first 40 minutes of cooling also suggest strong hysteresis expected for out of equilibria conditions typical for rapid cooling of aqueous solutions. The phase configuration stabilizes at approximately 209 MPa for each chamber. The final transition characteristics of pressure and temperature align with the pressure and temperature range of the ice-II region in the water phase diagram.

During the warming process we observe small pressure fluctuations that could correspond to formation of ice Ih from ice II or ice III, until the assemblage reaches starts to produce melt, as marked by a 'kink' in the pressure curve around the 1000 minute mark. This point marks the unique "cenotectic" point for each solution, after which the pressure decreases monotonically as the temperature increases, following the eutectic curve along the brine-ice Ih-KCl equilibrium line. Each step in this process takes 20 minutes, with approximately 2 of these minutes required to stabilize the temperature within the bath, which is increased in 0.5K increments. This stabilization period was chosen to ensure equilibration of each chamber sample with the surrounding bath temperature, which is confirmed by the stabilization of the pressure signal (as shown in the insets of Fig S2).

The temperature at which the system reaches atmospheric pressure corresponds to the eutectic temperature of the solution.

Supplementary Note 3: Additional data on solutions with apparent intermediate hydrates

For more details on P-T profiles in solutions with intermediate hydrates, Figures S3 - S5 below show every run recorded for the binary solutions found to produce intermediate high-pressure hydrate phases. General conclusions about the data shown here do not deviate from those presented in the main text, but we suspect that these additional data may be of interest to researchers studying any one of these solutions in greater depth.



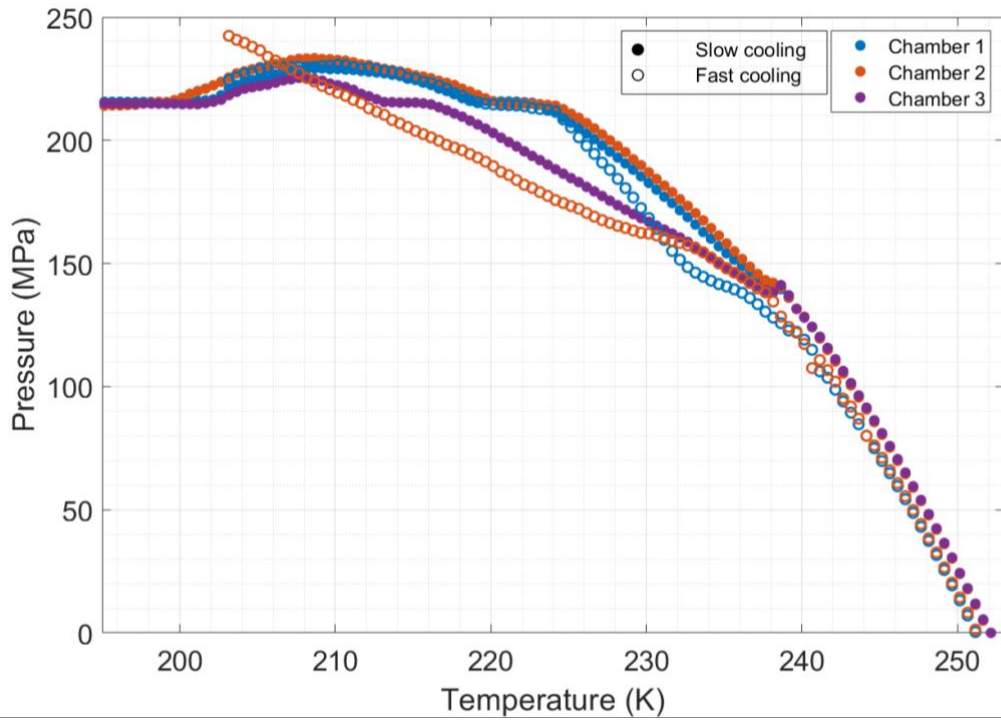
Supplementary Figure 3. All individual P-T curves recorded for NaHCO₃.

NaHCO₃ exhibited the greatest diversity of P-T transition features of the solutions considered, and as such, we experimented with additional cooling protocols in an effort to solicit more behaviors. In addition to the slow cooling and slow+fast cooling protocols described in the main text, we also tried two fast cooling protocols:

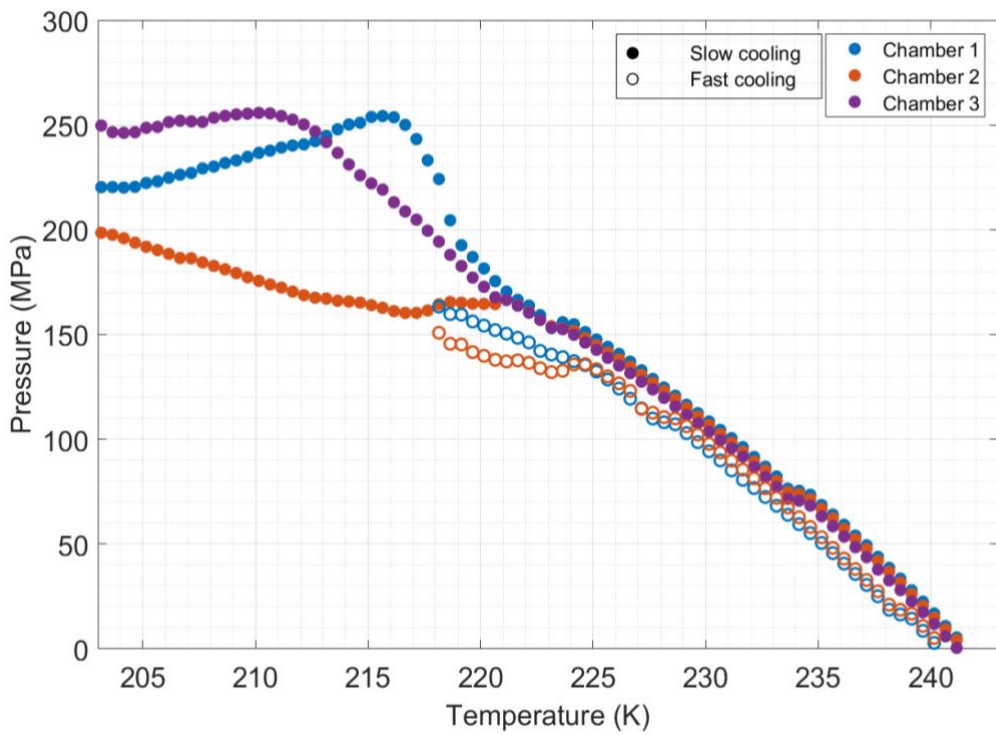
Fast Cooling 1: Submersion directly from room temperature to 213.15K.

Fast Cooling 2: Submersion directly from room temperature to 241.15K.

In Figure S3 above, it should be noted that the metastable phase configurations and byproducts produced during fast cooling appear to linger to higher temperatures than those for slow cooling. For these protocols, metastable byproducts appear to linger all the way to atmospheric pressure, affecting the recorded atmospheric pressure eutectic point, with greater deviation in eutectic temperature measured for greater cooling rate. While this phenomenon needs significantly more investigation in order to draw any firm conclusions, this behavior suggests that there *may* be metastable hydrates of NaHCO₃ that can persist at atmospheric temperature at around 273.15 K. These intermediate phases warrant further investigation, especially via metrological means that may produce more granular information on hydrate structure, such as x-ray diffraction or Raman spectroscopy.



Supplementary Figure 4. All individual P-T curves recorded for NaCl.



Supplementary Figure 5. All individual P-T curves recorded for MgCl₂.

Supplementary Note 4. Uncertainty analysis

Our uncertainty analysis employs the propagation of uncertainties for independent variables using the root sum squared (RSS) method, as detailed by Taylor⁸ and JCGM 100:2008⁹. Data presented in Figure 2 was obtained by measuring pressure at each steady temperature for every solution, as described in the methods section. The uncertainties in Figure 2a result from propagating the experimental standard deviation and the systematic error of the pressure sensors, which have an accuracy (NLHR) of 0.15% of span BFSL according to their data sheet. Temperature measurements were recorded via a calibration-grade Fluke thermocouple, and given its minimal systematic uncertainty (0.05°C), its effect was deemed negligible in our analysis.

The determination of the cenotectic point coordinates integrate the aforementioned uncertainties, as well as errors arising from polynomial curve fitting of the data. The phase transition at the cenotectic point, characterized by a discontinuity in the slope of the P-T curve of the solution, is mathematically defined as the intersection of the fitted polynomials. Due to measured uncertainties, this intersection point becomes a region, highlighted in Figure S6.

To ascertain the uncertainty region of the cenotectic point, the total uncertainty of the two fitted polynomials intersecting at the cenotectic point was calculated at each temperature increment. These uncertainties are considered independent, thus the total uncertainty at each temperature is the quadrature sum of the individual uncertainties, as follows:

$$\sigma_{total} = \sqrt{SEM^2 + (t\sigma_{fitting})^2 + \sigma_{device}^2} \quad (1)$$

where SEM is the experimental standard error of the mean, $\sigma_{fitting}$ is the uncertainty of the fitted polynomial, t is the t-distribution factor, and σ_{device} is the uncertainty of the pressure sensor.

In accordance with JCGM guidelines, SEM is calculated as:

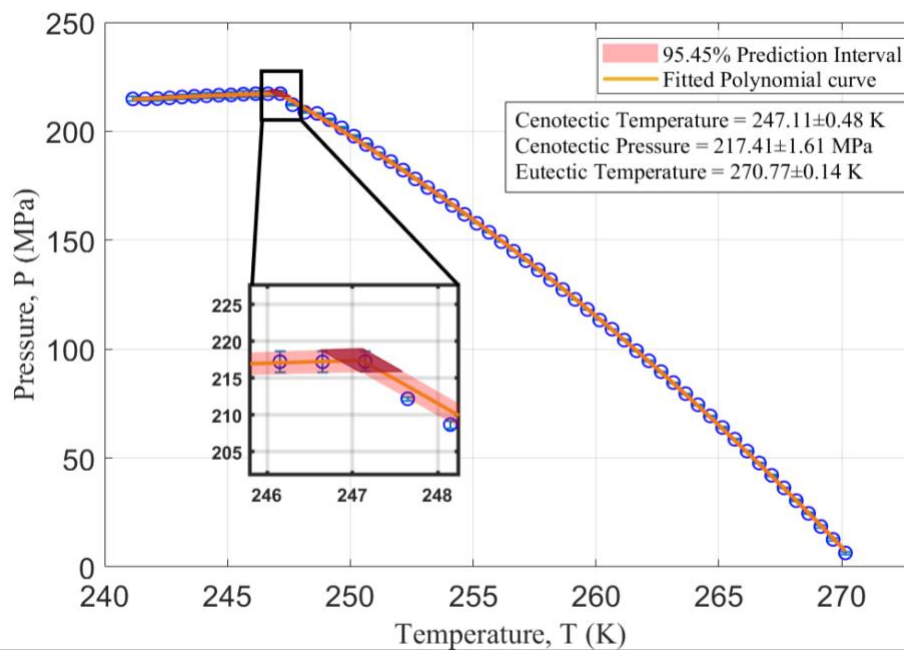
$$SEM = \frac{\sigma}{\sqrt{N}} \quad (2)$$

Where σ is the standard deviation of the measured pressure data at each temperature, and N is the number of technical replicates in each experiment, which, in this case, was 3 per solution. The uncertainty of the fitted polynomials before and after the cenotectic point was calculated using MATLAB's internal fit uncertainty algorithm, as evaluated from the polyfit() and polyval() functions. The t-distribution factor, as per JCGM recommendations, is determined based on the degrees of

freedom in the system and the desired confidence level, set at 95.45% in this study. Therefore, with 3 sensors at each experiment, the t-distribution factor of 3.31 was used. Device uncertainty was derived from the NLHR accuracy specified in the ESI datasheet for the 0-4000 bar pressure sensors (<0.15% BFSL), assumed to be constant with temperature.

By computing the total uncertainty of the fitted polynomials, the intersection of their upper and lower bounds was identified, delineating the uncertainty zone of the cenotectic point in the P-T diagram. Thus, uncertainty in cenotectic pressure is reported as the maximum vertical difference between any two points in this uncertainty zone, and uncertainty in cenotectic temperature is reported as the maximum horizontal difference between any two points in the same.

Similarly, the uncertainty of the eutectic temperature is determined by the difference between the upper and lower bounds of the intersection of the final fitted polynomial with 0.1 MPa in the diagram. Table 1 presents the calculated uncertainties of the cenotectic and eutectic characteristics for each tested solution.



Supplementary Figure 6. The uncertainty analysis on the cenotectic point for Na_2CO_3 solution

Supplementary Note 5: Definition of the cenotectic point in the context of Gibbs' Phase Rule

In order to aid future study of the cenotectic point, we provide in this note additional description of its definition in the context of Gibbs Phase Rule.

Per the definition in the main text, *the cenotectic is the invariant point occurring at the lowest temperature at which the liquid phase, for any value of concentration, pressure, or other thermodynamic forces acting on the system, remains in stable equilibrium.*

Gibbs Phase Rule offers some additional insight into the cenotectic point, by prescribing how many phases may be present at an any invariant point in a given system. For simple systems unaffected by modes of thermodynamic work other than mechanical (PV), thermal (TS), and chemical (μN) work, Gibbs Phase Rule gives: $F = C - P + 2$, wherein F is the number of intensive thermodynamic degrees of freedom, C is the number of chemical components in solution, and P is the number of phases present. Invariant points such as the cenotectic are defined $F = 0$ degrees of freedom, and as such, the number of phases present at the cenotectic P_K may be calculated as $P = C + 2$. For example, in the simple binary ($C = 2$) solutions investigated in this work, there will be $P = 4$ phases present at the cenotectic (i.e. the brine, ice-Ih, ice II/III, and the solute-bearing solid phase).

If the system *is* under the influence of non-simple forms of thermodynamic work, such as electrical work (EP) or magnetic work (BM), the Generalized Gibbs Phase Rule must be applied instead: $F = W - P + 1$, wherein W is the number of *independent* thermodynamic conjugate variable pairs (i.e. modes of thermodynamic work) contributing to the free energy of the system. Thus, the number of phases present at the cenotectic in a non-simple system is given by $P = W + 1$. For example, in a binary solution also under the influence of electrical work (i.e. exposed to an electrical field), $W = (PV, TS, \mu N, EP) = 4$, and there will thus be $P = 5$ phases present at the cenotectic.

As such, a more rigorous mathematical definition of the cenotectic temperature specifically may be provided in terms of the Generalized Gibbs Phase Rule:

For any system affected by W independent modes of thermodynamic work, there exists some set of invariant point temperatures IPT at which $W+1$ phases coexist, and the cenotectic temperature T_k is the minimum of this set:

$$T_k = \min\{IPT\}$$

Given that $W+1$ phases can only coexist at invariant points for which there are 0 intensive thermodynamic degrees of freedom, the cenotectic pressure (or the value of any other intensive variable at the cenotectic point) may be defined circularly as the

pressure corresponding to the cenotectic temperature, i.e., the point is fully prescribed by its temperature.

Supplementary References:

1. Pascual, M. R., Trambitas, D., Calvo, E. S., Kramer, H. & Witkamp, G. J. Determination of the eutectic solubility lines of the ternary system NaHCO₃-Na₂CO₃-H₂O. *Chemical Engineering Research and Design* **88**, (2010).
2. Li, G., Hwang, Y., Radermacher, R. & Chun, H. H. Review of cold storage materials for subzero applications. *Energy* vol. 51 Preprint at <https://doi.org/10.1016/j.energy.2012.12.002> (2013).
3. Pillay, V. *et al.* MgSO₄ + H₂O system at eutectic conditions and thermodynamic solubility products of MgSO₄·12H₂O(s) and MgSO₄·7H₂O(s). *J Chem Eng Data* **50**, (2005).
4. Yuan, L. *et al.* Precise Urea/Water Eutectic Composition by Temperature-Resolved Second Harmonic Generation. *Chem Eng Technol* **39**, (2016).
5. González Díaz, C. *et al.* Thermal conductivity measurements of macroscopic frozen salt ice analogues of Jovian icy moons in support of the planned JUICE mission. *Mon Not R Astron Soc* **510**, (2022).
6. Journaux, B. *et al.* On the identification of hyperhydrated sodium chloride hydrates, stable at icy moon conditions. *Proc Natl Acad Sci U S A* **120**, (2023).
7. Ketcham, S. A., Minsk, L. D., Blackburn, R. R. & Fleege, E. J. Anti-icing: Lower the cost of safer roads. *Public Works* **128**, (1997).
8. Taylor, J. R. An Introduction to Error Analysis. *Journal of the Acoustical Society of America* **101**, (1997).
9. JCGM 100. JCGM 100:2008 - Evaluation of measurement data - Guide to the expression of uncertainty in measurement. *International Organization for Standardization Geneva ISBN* **50**, (2008).